Experiments in Fluids (2022) 63:86
https://doi.org/10.1007/s00348-022-03416-7

RESEARCH ARTICLE

3D visualization of droplet splash dynamics with high-speed digital holography

Xiaodan Lin[1] · **Qiao Wang**[2] · **Yingchun Wu**[1] · **Longchao Yao**[1] · **Zhiliang Xue**[1] · **Xuecheng Wu**[1]

Received: 11 June 2021 / Revised: 9 March 2022 / Accepted: 10 March 2022 / Published online: 16 May 2022

Abstract

Three-dimensional (3D) visualization on droplet splashing characteristics is of great importance in the research of droplet impact on a solid surface. In this study, a high-speed digital in-line holography (DIH) system with 1024 × 1024 pixels at 3500 Hz is employed to investigate the 3D splashing characteristics of large droplet impact (2630 ± 20 μm, which is called the mother droplet) on different rough surfaces and impacting velocities. The experiments are carried out in a wind tunnel at room temperature (15 °C). The high-speed DIH system is calibrated to show that the depth position measurement error is less than 70 μm, and the the size measurement error is less than 2.06% for the target object larger than 31.1 μm. The droplet sizes, droplet number distribution, 3D position of the daughter droplets generated from droplet splash, as well as the morphology evolution are captured by time-resolved holographic visualization. The 3D motion trajectory of the daughter droplets is obtained by applying a four consecutive frames particle tracking algorithm based on particle matching probability, which can help to predict the secondary impact points of the daughter droplets. The results show that there exist three kinds of droplet breakup modes during the droplet impact and splashing process. It presents a more violent splashing behavior with the surface roughness and impacting velocity. The number of the daughter droplets at the 3rd frame after droplet collision increases with the surface roughness, which are 104, 49, 39, and 38 when the surface roughnesses are 250 μm, 25 μm, 3.2 μm and 2.6 μm, respectively. The daughter droplets are not in radially symmetric distribution for the reason of an asymmetry distribution of the flow field along the *x*-axis and *y*-axis in the test zone of the wind tunnel. High-speed DIH can be a tool to investigate the splashing characteristics to support the 3D splashing model improvement.

Graphical abstract

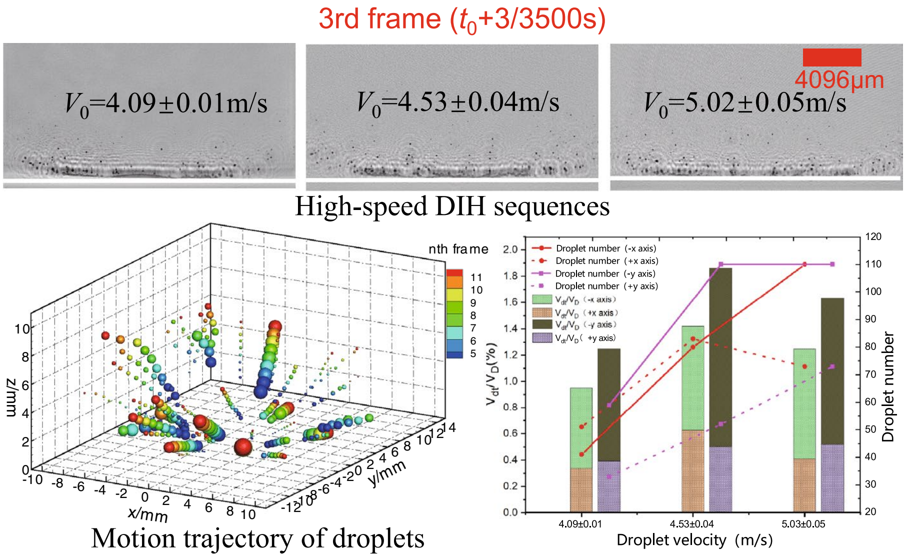

Extended author information available on the last page of the article

1 Introduction

Droplet impact on a solid surface is a key element of a wide variety of phenomena encountered in different fields. In nature, raindrops impinge on the surfaces of plants Liu et al. (2015) and soil Wischmeier and Smith (1958). In technical and industrial applications, it is widely used in ink-jet printing Zable (1977), liquid fuel combustion Wang et al. (2004), the design of functional surfaces for self-cleaning Liu and Jiang (2012); Blossey (2003), spray cooling Kim (2007), and forensic researches Adam (2013). When a droplet impacts on a solid and dry surface, it will deposit on the surface to form a liquid film, or splash and form daughter droplets under a more energetic impact Yarin (2006). Droplet splash results from the combined action of gas, solid and liquid phases. Thus, the properties of droplet, impacting surface and surrounding gas are three important factors that affect droplet splashing process. The droplet properties include droplet size Villermaux and Bossa (2011), viscosity Scheller and Bousfield (1995), density Scheller and Bousfield (1995) and velocity Thoroddsen et al. (2012); the impacting surface properties refer to surface wettability de Goede et al. (2021); Wang et al. (2009), surface roughness Tang et al. (2017); Xu et al. (2007), surface temperature Khavari et al. (2015); Potapczuk (2003), motion velocity Hao and Green (2017), and the inclination angle of the surface Roisman et al. (2008); Biroun et al. (2020). In addition, the surrounding gas properties also have significant influence, such as the pressure Latka et al. (2012) and molecular weight Xu et al. (2005) of the gas.

This so-called splashing phenomenon has been the subject of numerous experimental studies for the last several decades. Worthington was one of the first researchers to investigate the droplet splashing process systematically Worthington (1877). Rioboo et al. (2001) used a CCD (Charged Coupled Device) camera with a resolution of low frame rate to record the splashing phenomenon of water droplets, ethanol droplets, and droplets of a mixture of glycerol and water impacting on a solid wall. The result showed that an increase in liquid viscosity will suppresses droplet splash, but the effect of viscosity on droplet splash is non-monotonic Vander Wal et al. (2006). Due to the limitation of the recording system with low frame rate, a timing control system needed to be arranged to obtain the transient droplet splashing images. With the rapid development of high-speed camera, high-speed photography shows its advantages on droplet splashing investigation. Range and Feuillebois (1998) experimentally studied the influence of surface roughness on liquid drop impact using a shadowgraph method with a rapid CCD camera. Koch and Grichnik (2016) focused on the effects of surface structure and chemical composition on droplet splash with the help of high-speed photography, and found that the application of hydrophile on the surface could effectively inhibit droplet splash. Latka et al. (2012) found that the lower air pressure suppressed droplet ejection not only during thin sheet formation but also for the prompt splash with high-speed imaging. High-speed photography can effectively present the evolution of droplet impact and splashing process. However, it is a 2D (two-dimensional) imaging technique with a limitation of camera depth of field. The 3D (three-dimensional) evolution of the droplet structure after droplet impact can not be observed to accurately investigate the droplet splashing characteristics. So it is important to develop a 3D visualization system for a qualitative and quantitative analysis of the daughter droplets.

Digital inline holography (DIH) is a real 3D imaging technique, which is capable of capturing the size, concentration, morphology, 3D position, and 3D velocity of particles Wu et al. (2015, 2016). DIH has been applied successfully in droplet fragmentation Yao et al. (2015), coal and aluminum particle combustion Lin et al. (2019); Wu et al. (2019); Gao et al. (2013), cloud particle detection Henneberger et al. (2013), etc. In this study, the water droplet impact and splash were 3D visualized with high-speed DIH system operated at 3500 Hz. The experiments were conducted in a wind tunnel at room temperature. The influences of the parameters that can affect the splashing mechanism, such as the surface roughness and droplet impacting velocity, were studied by analyzing the size, 3D position, and 3D motion trajectories of the daughter droplets under different experimental conditions.

2 Experiment methodology

2.1 Experimental setup

The droplet impact and splashing investigation was conducted in a 0.3 m × 0.2 m wind tunnel with a high-speed DIH system. Fig. 1a shows the schematic of the experimental facility, including a wind tunnel, a droplet generator system, and a high-speed DIH visualization system. The test zone of the wind tunnel was 0.3 m long, 0.075 m wide, and 0.2 m high. A variable frequency drive was applied to control a fan motor to obtain a linear variation of airspeed. Experiments were operated at room temperature, 15 °C. A mono-dispersed droplet generator was used to produce the test water droplet. The diameter of the droplet was controlled by a syringe needle, and the flow rate of water was supplied by an injection pump with 3.0 mL/h of the injection flow rate. The droplet generator was installed in a stable section, so the droplet can be accelerated to the desired velocity through the contractive section. An aluminum block with different surface roughnesses was positioned near the bottom of the test section, on which the accelerated droplet impacted. The droplet produced from the drop generator

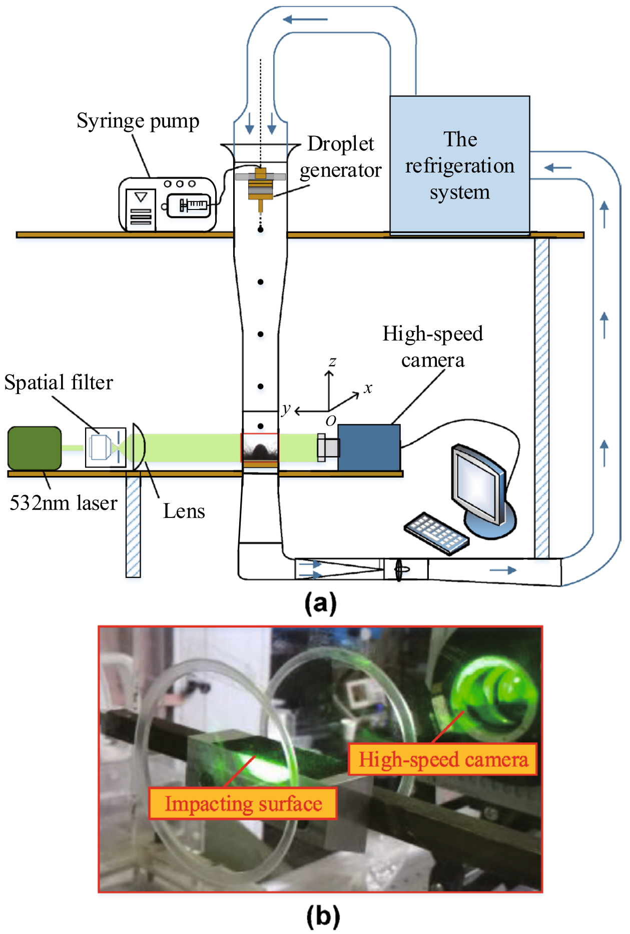

Fig. 1 Experimental configuration of high-speed DIH measurement of droplet impact. **a** overall diagram of the experimental setup; **b** details of the test zone

is named as the mother droplet, and the droplets generated after droplet impact are called as the daughter droplets. The definition of the 3D axis for droplets' 3D position is also demonstrated in Fig. 1a. It is noted that the negative direction of the y-axis points to the direction of the camera. O is the origin of the coordinate system, which is also the impact point of the mother droplet. The details of the test zone are displayed in Fig. 1b.

As to the optical setup of the high-speed DIH system, a continuous wave laser (Oxxius LCX-532S-300, $\lambda = 532$ nm) was attenuated using a neutral density filter to avoid pixel saturation in the camera senor. Then it was spatially filtered, expanded, and collimated to a plane wave with a diameter of about 50 mm. When the plane wave traveled through the test section, the light scattered by the droplets was called object wave, while the undisturbed part served as reference wave. The object wave interfered with the reference wave to produce a hologram of droplets directly recorded by a Lavision high-speed camera with the resolution of 1024 × 1024 pixels operated at 3500 Hz with an exposure time of 3 μs. The recording field of view for the high-speed DIH system was 20.48 mm × 20.48 mm. The distribution of the daughter droplets was relatively sparse (≤ 200 particles in a holographic image), which was suitable for the DIH measurement.

2.2 Test conditions

All the seven test cases in this study are listed in Table 1. Every case was repeated by 5 times. The droplet diameters in these cases were 2630 ± 20 μm. The impacting velocities of the droplets were designed to about 4.09 ± 0.01 m/s, 4.53 ± 0.04 m/s, and 5.02 ± 0.05 m/s. The different surface roughnesses were prepared with different sandpapers covering on the aluminum surface, which were 250 μm, 25 μm, 3.2 μm, and 2.6 μm, respectively. In this paper, surface roughness Ra referred to the arithmetic mean of the absolute values of vertical deviation from the mean line through the surface profile Bhushan (2000). Past researches have concluded that water droplet impact process was mainly controlled by the following dimensionless parameters, including Weber number ($We = \rho D V_0^2/\sigma$), Reynolds number ($Re = \rho D V_0/\mu$) and Mundo impact parameter ($K = Oh \cdot Re^{1.25}$), where ρ, μ and σ were the liquid density, the viscosity and the surface tension for the liquid droplet respectively Khojasteh et al. (2016). D and V_0 were the diameter and impacting velocity of the mother droplet respectively. Mundo impact parameter K was used to describe an empirical relationship between no-splash and splash transition with the effect of surface roughness. In the study of Mundo, the droplet splashing phenomenon happened when K was larger than 57.7 Mundo et al. (1995). As shown in

Table 1 Conditions of the representative cases for water droplet impact investigation

Cases	D (μm)	V_0 (m/s)	Ra (μm)	We	Re	K
1	2630 ± 20 μm	4.09 ± 0.01	250	598	9419	241
2	2630 ± 20 μm	4.09 ± 0.01	25	598	9419	241
3	2630 ± 20 μm	4.09 ± 0.01	3.2	598	9419	241
4	2630 ± 20 μm	4.09 ± 0.01	2.6	598	9419	241
5	2630 ± 20 μm	4.53 ± 0.04	25	706	10036	266
6	2630 ± 20 μm	5.02 ± 0.05	25	850	10901	298

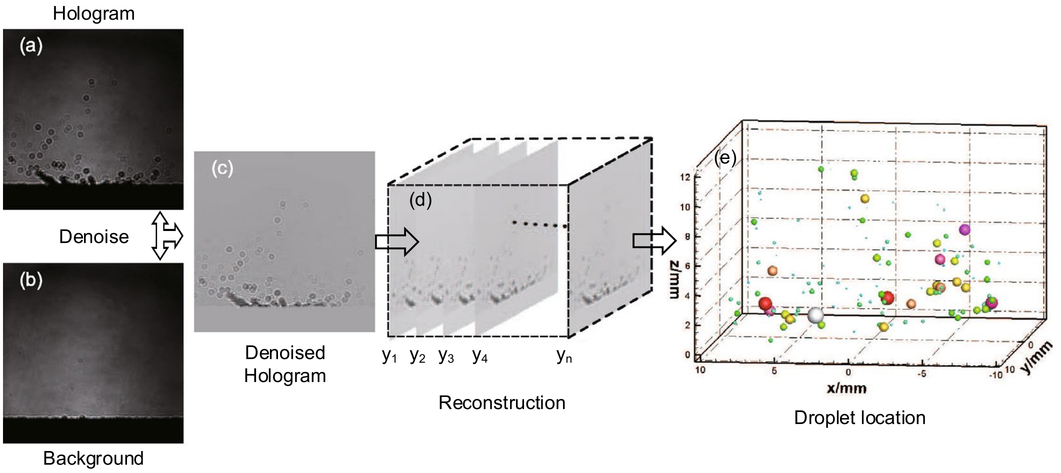

Fig. 2 The data process with high-speed DIH

Table 1, the corresponding K for all cases were large enough to prompt the droplet splash.

2.3 Data processing

Compared to high-speed photography, DIH has distinct advantages in the 3D visualization of drop impact and splash. This technology can record the amplitude and phase of the droplets in the form of interference fringes, that was the hologram as mentioned above. The specific principle was as follows:

$$I_{\mathrm{H}} = |\mathbf{E}_{\mathrm{O}} + E_{\mathrm{R}}|^2 = |\mathbf{E}_{\mathrm{O}}|^2 + |\mathbf{E}_{\mathrm{R}}|^2 + \mathbf{E}_{\mathrm{O}}\mathbf{E}_{\mathrm{R}}^* + \mathbf{E}_{\mathrm{O}}^*\mathbf{E}_{\mathrm{R}} \quad (1)$$

where E_{R} and E_{O} referred to the reference wave and object wave, and E_{R}^* and E_{O}^* were the conjugation wave of the reference wave and object wave.

Then DIH can reveal the 3D position of the droplets by inverting the phase information of the droplets. The detailed processing procedure of droplet hologram was introduced in Fig. 2. The recorded hologram (Fig. 2a) was firstly denoised with the algorithm of background abstract (Fig. 2b) to improve the image quality and also eliminate the influence of the solid surface, as shown in the denoised hologram, Fig. 2c. Then the denoised hologram was volumetrically reconstructed along the y-axis (y-axis is the depth location) slice by slice by using the Fresnel-Kirchhoff integral, as shown in Eq. (2),

$$E\left(x', y', z'\right) = \frac{1}{\mathrm{j}\lambda} \int \int_{\infty} I_H(\xi, \eta) \frac{\exp\left[\mathrm{j}\frac{2\pi}{\lambda}\sqrt{(\xi - x')^2 + (\eta - z')^2 + (y')^2}\right]}{\sqrt{(\xi - x')^2 + (\eta - z')^2 + (y')^2}} \mathrm{d}\xi \mathrm{d}\eta \quad (2)$$

where (ξ, η) and (x', z') were the coordinates of the hologram plane and reconstruction plane respectively, y' was the reconstruction distance, λ was the wavelength, and j was imaginary unit. Secondly, the reconstructed image slices were synthesized to an extended field image (EFI) with a wavelet-based image fusion algorithm Yingchun et al. (2014), where all droplets in the reconstructed volume were focalized. The droplets were detected by applying a gray-scale threshold to the EFI. Finally, the locations of the droplets along the y-axis were determined with focus metrics in Fig. 2e, which was related to the variance of the intensity gradient in the vicinity of the droplets. Therefore, the droplet size, 2D morphology, and 3D position of the droplets were retrieved. The detailed introduction for the selection of the threshold, the definition of the focus metrics, and the measurement accuracy of the algorithm were reported in our previous work Yao et al. (2015).

2.4 DIH system calibration

The effectiveness and accuracy of the DIH system for measuring the object size and spatial localization were validated with a calibration target, that is the USAF1951 resolution plate, as shown in Fig. 3a. The calibration target consisted of different calibration bars with specific width. For example, the width of the calibration bar marked with a red rectangle in Fig. 3a is 125 μm. Then the measurement accuracy of the DIH system can be calibrated by recording the width of the target calibration bars with different sizes in different depth locations (along y-axis). Since the distance between the calibration target and the recording plane of the camera was difficult to be precisely determined by manual measurement, the calibration target was moved sequentially by 2 mm to obtain the measurement accuracy of the relative depth position of the DIH system, which will not affect the analysis

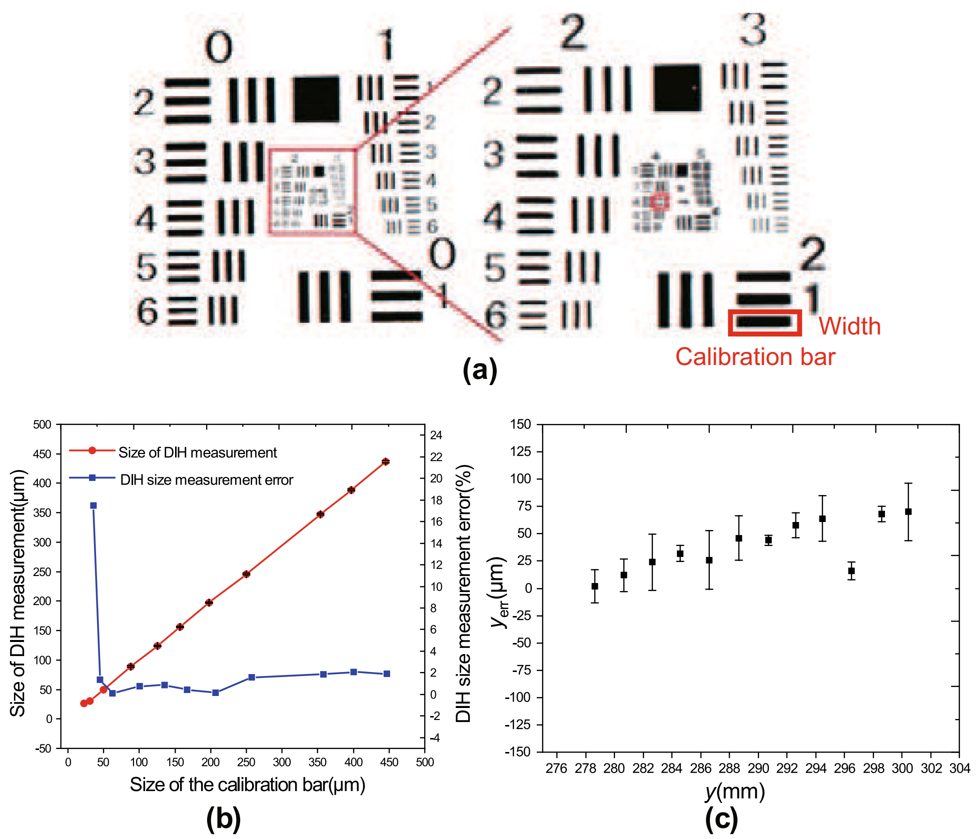

Fig. 3 The details of the calibration target and the calibration results. **a** calibration target; **b** size measurement error; **c** depth position measurement error

of the droplet impact and splashing process. The calibration target was installed on a 3D motorized liner stage for an accurate movement. The recording distances of the daughter droplets were in the range of 22.5–30.0 cm from the camera, and the measurement accuracy of the DIH system generally decreases with the recording distance. So the calibration target was placed at about 278–302 mm away from the recording plane of the camera. The camera resolution of this calibration system is 1024 × 1024 pixels and the pixel size is 20 μm , which is consistent with the parameters of the high-speed DIH system in Fig. 1a. The calibration experiments were repeated by 5 times. The results are shown in Fig. 3b and c. Figure 3b presents the size mesurement error of the DIH system at $y = 278.6$ mm, and Fig. 3c displays the depth position measurement error for the calibration bar with 125 μm width. It can be seen that the size measurement error is less than 2.06% when the object size is larger than 31.1 μm, and the size measurement error sharply increases to 17.46% when the object size is 22.1 μm, which results from the limitation of the camera resolution. However, the difference between the measurement result and the actual size is only 3.9 μm. As to the depth position measurement error, it slowly increases with the recording distance. When the recording distance is less than 290.6 mm, the object localization error is less than 50 μm. Within the target recording distances, the depth position measurement error of the DIH system is less than 70 μm. This is acceptable and effective for the particle localization and size measurement of the splashing daughter droplets during droplet impact.

To sum up, the high-speed DIH system, which is equipped with a continuous wave laser with 532 nm and a high-speed camera with 1024 × 1024 pixels and 20 μm pixel size, has been proved its validity and reliability in measuring the object size and spatial localization. For the target object larger than 31.1 μm placed at ≤ 302 mm away from the recording plane of the camera, the depth position measurement error is less than 70 μm, and the the size measurement error is less than 2.06%.

2.5 Comparison on high-speed DIH system with high-speed photography

As said, high-speed photography is a useful technology to investigate droplet impact and splash. However, it is a 2D imaging technique with a limitation of camera depth of field, and only can get the 2D silhouettes in different views. The measurement comparison between high-speed DIH system and high-speed photography is displayed to show the distinct advantages of DIH measurement in Fig. 4. The high-speed camera applied and the recording field of view for the high-speed DIH system are the same as those of the high-speed photography. The diameter of the mother droplet is 2630 ± 20 μm, and the surface roughness is 250 μm with the impacting velocity 4.09 ± 0.01 m/s. The results show that DIH can help to guarantee all daughter droplets and liquid film in focus compared to high-speed photography. The spatially dispersed daughter droplets are easily out of focus in Fig. 4b captured by high-speed photography, which seriously affects the accurate measurement of the particle size, morphology, number, velocities of the daughter droplets.

3 Results and discussions

3.1 Analysis of experimental repeatability

Five repeated experiments of case 1 were conducted and analyzed to verify the repeatability of the experiments. The roughness of the surface was 250 μm, and the impacting velocity of the mother droplet was 4.09 ± 0.01 m/s. Then, the repeatability and reliability of the repeated results were verified by comparison of the probability density distribution of the daughter droplets at the 6th frame of the recording holographic images. It is noted that the image where the mother droplet firstly hits the solid surface is set as 0 frame. Then the 6th frame represents the 6th holographic picture after 0 frame. The time interval between two consecutive frames is 1/3500 s. The result of analysis is shown in Fig. 5, where *d* means the diameter of the daughter droplets. It can be seen that all five repeated experiments show almost the same trend in terms of the probability density distribution at the 6th frame. The result shows good repeatability of the DIH measurement.

3.2 Droplet splashing dynamics with high-speed DIH imaging

Figure 6 presents a high-speed DIH sequence of droplet impact and splash at case 1 reconstructed from holograms, where the mother droplet diameter is 2630 ± 20 μm. The droplet maintains its sphericity at the -1st frame before impacting on the surface. When it hits the solid surface, the top of the mother droplet still keeps round, while the bottom of the droplet shows the initial compaction on the solid surface and deforms axisymmetrically. A liquid lamella begins to be expelled along with the radial position where the droplet contacts the solid surface after one frame. When the expansion rate of the liquid lamella slows down, the liquid lamella later takes the shape of a thin liquid sheet with an unstable free rim, as shown in the inset at the 1st frame. When disturbed, the free rim inevitably forms cusps or even jets in the inset at the 2nd frame. Then the cusps of the free rim start to rupture and produce numerous small daughter droplets, which is called droplet breakup mode 1. While these jets break up into some small droplets and large droplets due to the capillary breakup mechanism named droplet breakup mode 2. After a few milliseconds, the liquid lamella can detach from the wall, resulting in the generation of the liquid filaments marked with the purple rectangle, which almost rupture into large droplets at the 12th frame. The liquid crush process is denominated as droplet breakup mode 3. Finally, the daughter droplets gradually move out of the camera field of view. The DIH sequences present droplet impact and splashing process with all droplets and irregular stuff focalized in the 3D space. The dynamic movement of the daughter droplets in 3D space can be seen in the additional information named as “droplet splashing process in 3D space”.

To analyze the change of droplet number and diameter of the daughter droplets with time, the droplet number of the daughter droplets with different diameters are accounted at 8 different time. It is important to note that the irregular liquid rims and filaments are ignored during the process of extracting the daughter droplets. Figure 7 presents the droplet number and the corresponding cumulative number distribution of the daughter droplets with time for Fig. 6. It can be seen that the size ranges of the daughter droplets get gradually larger with time before the 8th frame. The droplet size range at the 2nd frame is from 25 to 227 μm. After one frame, the largest droplet size increases to 260 μm, which are 355 μm, 374 μm, and 393 μm at the 4th frame, the 5th frame, and the 8th frame, respectively. There are about 33 small daughter droplets in the range of around 50–70 μm. After a few milliseconds, the droplet ejection from the cusps of the free rim in droplet breakup mode 1 and the jets of free rim in droplet breakup mode 2 result in the increase of the

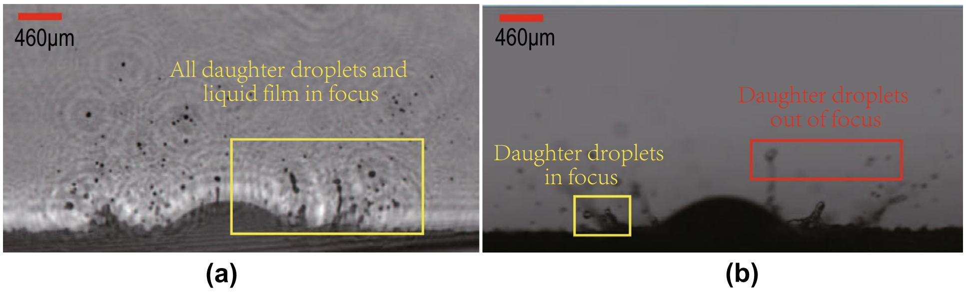

Fig. 4 The measurement comparison on high-speed DIH system with high-speed photography under case 1 conditions: $D = 2630 \pm 20$ μm, $V_0 = 4.09 \pm 0.01$ m/s, and $Ra = 250$ μm. **a** image with high-speed DIH system; **b** image with high-speed photography

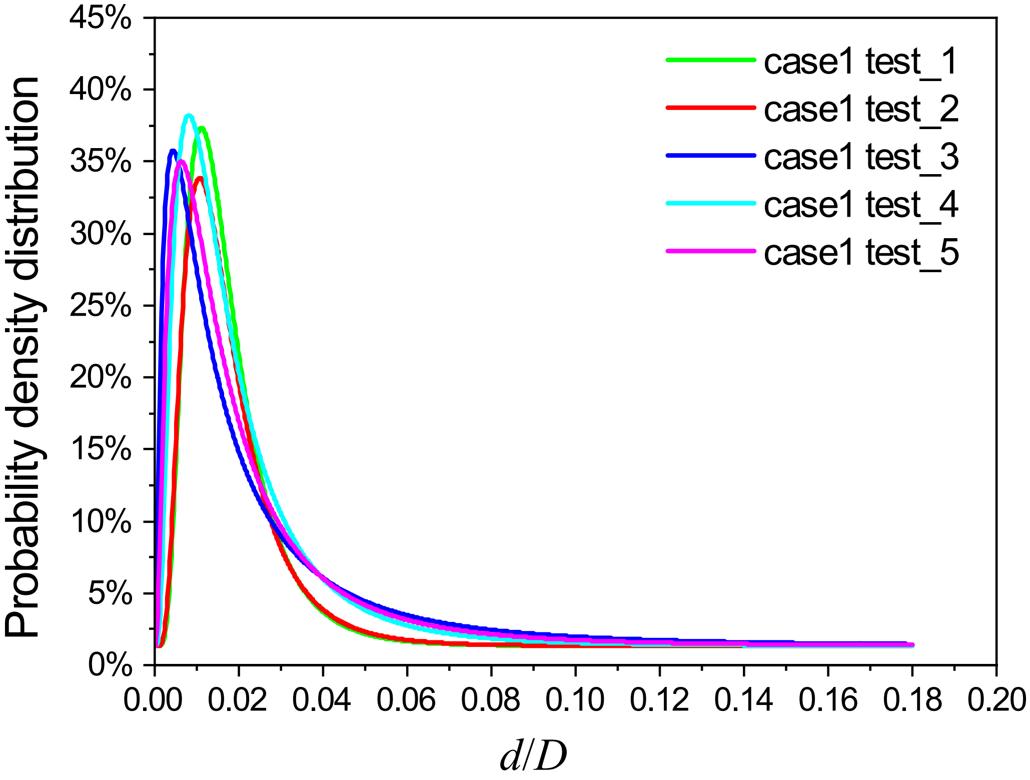

Fig. 5 Probability density distribution of the daughter droplets with five repeated experiments at the 6th frame under case 1 conditions: D=2630 ± 20 μm, V_0=4.09 ± 0.01 m/s, and Ra=250 μm

number of small daughter droplets to 43 at the 3rd frame, 48 at the 4th frame, 49 at the 5th frame, and 53 at the 8th frame. The number of the large droplets also increases coming from the rupture of the jets of free rim in droplet breakup mode 2. The droplet numbers at the diameter of around 146 μm are 7 at the 2nd frame and 9 at the 3rd frame, respectively. When it comes to the next three moments, the large droplets crush to increase the number of small droplets, and the number of the relatively large droplets of around 127 μm also obviously increases to 10 at the 4th frame, 13 at the 5th frame, and 17 at the 8th frame. At the 8th frame, more irregular liquid filaments rupture into more large droplets in the range of 203–222 μm and 260–279 μm in droplet breakup mode 3. The number of the daughter droplets gradually increases at these 5 time with the total number of 73, 112, 125, 133 and 164 respectively. At the 12th frame, the diameter range grows from 25 to 1000 μm when a large liquid filament breaks up into a few big parts in droplet breakup mode 3. From this time, the total droplet number keeps essentially constant with the number of about 180. The marked large droplets with the red rectangle and the blue rectangle in Fig. 7b are the same daughter droplet. They show different morphologies and droplet sizes of 398 μm at the 16th frame and 462 μm at the 18th frame for the reason that the daughter droplet is rotating in the air over time.

The 3D motion trajectory of the daughter droplets is displayed in Fig. 8. A four consecutive frames particle tracking algorithm based on particle matching probability Heyman (2019) is applied to trace the change of 3D position of the daughter droplet with time from the 5th frame to the 11th frame. The color of the daughter droplets indicates the frame in which the particle is located. The morphologies of the daughter droplets are evolving during the splashing process. What's more, some daughter droplets will be out of the view of the high-speed camera in these 7 frames. So there are only 49 daughter droplets detected at this case. Figure 8 shows that the trajectory of the daughter droplets is almost linearly distributed in 3D space, which is slightly influenced by gravity. The 3D motion tracking of particles will help to predict the secondary impact points of the daughter droplets, and can support to validate the simulation results with 3D splashing models. The animation of the daughter droplets with 3D motion trajectory can be seen in the additional information named as "The 3D motion trajectory of the daughter droplets".

3.3 Influence of surface roughness

In this section, the evolution in the splashing behavior with different surface roughnesses are compared in Fig. 9 to

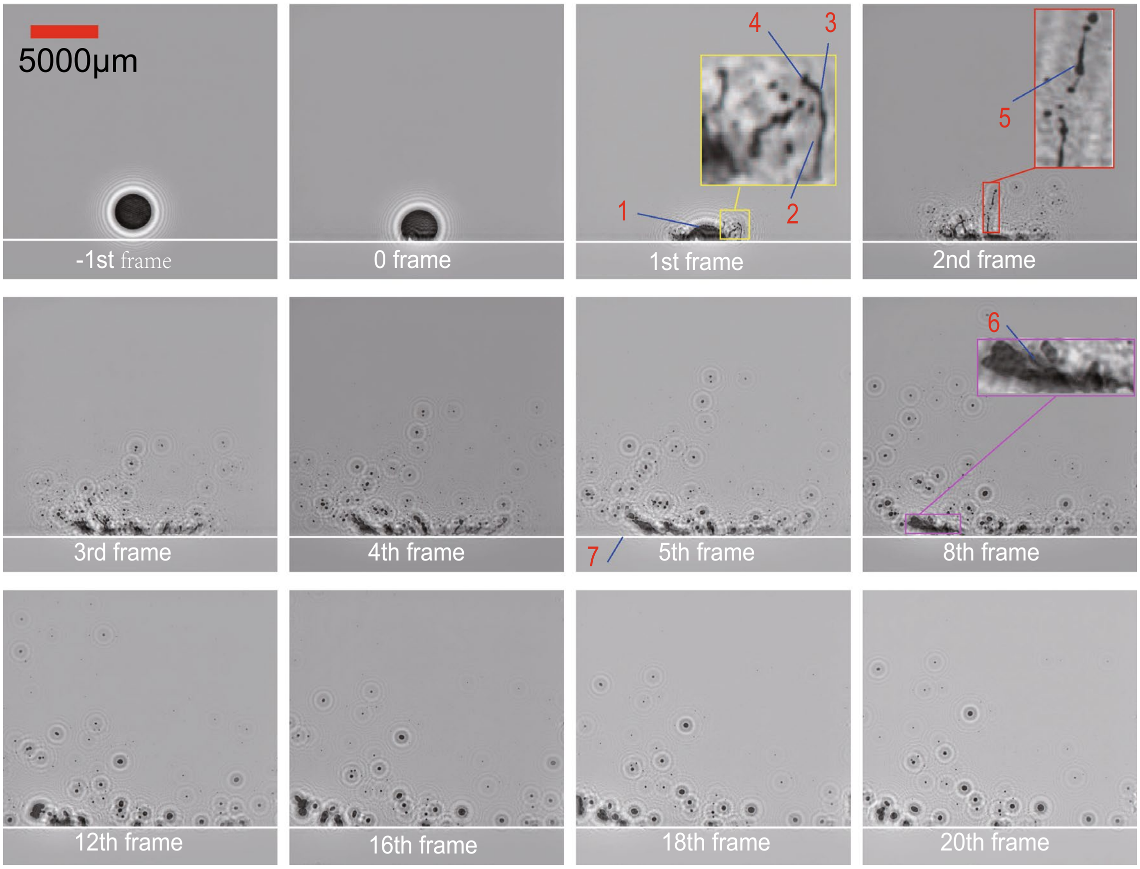

Fig. 6 The high-speed DIH sequence of droplet impact and splashing process under case 1 conditions: $D = 2630 \pm 20$ μm, $V_0 = 4.09 \pm 0.01$ m/s, and $Ra = 250$ μm: 1, residual top of mother droplet; 2, liquid thin sheet; 3, free rim; 4, cusps of free rim; 5, jets of free rim; 6, liquid filaments; 7, wall

investigate the influence of surface roughness on droplet splashing process. The droplet impacting velocities at all experiment cases are 4.09 ± 0.01 m/s, and the surface roughnesses for case 1, case 2, case 3 and case 4 are 250 μm, 25 μm, 3.2 μm, and 2.6 μm respectively. The corresponding K for all cases is 241, which means that the splashing phenomena will occur at these four cases. Each column of pictures stands for the droplet impact and splashing process with the high-speed DIH for one case.

There is a clear difference during droplet impact and splashing process for the four experimental cases. On a rough surface, the mother droplets impact and break up into numerous small and large daughter droplets. The number of the daughter droplets increases with the surface roughness, which are 111, 57, 38 and 29 at case 1 with 250 μm, case 2 with 25 μm, case 3 with 3.2 μm and case 4 with 2.6 μm at the 5th frame. This is because the size of the particles of abrading materials embedded in the sandpaper is more coarse for the rougher surfaces, which contributes to a deeper depression between the particles of abrading materials embedded in the surface. Then the tangential obstruction increases with the surface roughness to hinder the spread of droplets on the surface. Driven by the counterforce, the daughter droplets are flying closer to the normal direction. So there exist more daughter droplets resulted from the rupture of cusps or jets of free rim and liquid filaments. The liquid filaments generated from droplet splash are more striking and irregular at case 1 with the surface roughness of 250 μm. It is obvious that the larger the surface roughness is, the higher the splashing heights of the daughter droplets are at the same recorded time. So it is indicated that the morphology evolution of the daughter droplets during impacting a rougher surface presents a more violent splashing behavior.

Figure 10 presents the number density of the daughter droplets at case 1, case 2, case 3, and case 4 at the 3rd frame. The size of the daughter droplets at these four cases are almost in the range of 25–247 μm, 25–236 μm, 25–251 μm, and 25–223 μm, respectively. As to the number of the daughter droplets, there are 104, 49, 39, 38 droplets generated from the droplet splashing on the surface with the roughness of 250 μm, 25 μm, 3.2 μm, and 2.6 μm. The number density of the daughter droplets for case 1 reaches 2 peak

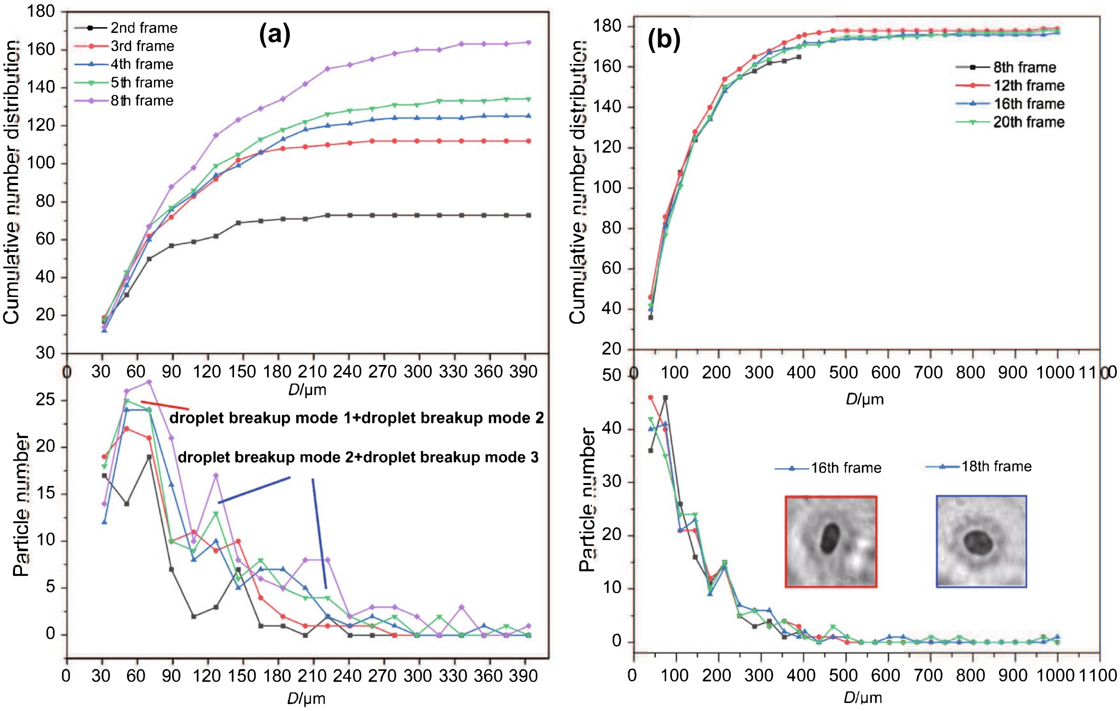

Fig. 7 The droplet number and the corresponding cumulative number distribution of the daughter droplets with time for Fig. 6

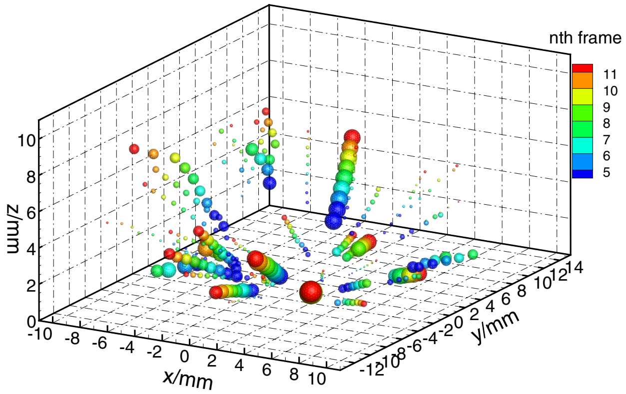

Fig. 8 The motion trajectory of the daughter droplets

values with 27 at $d_1 = 25$ μm and 14 at $d_2 = 105$ μm. For other cases with smoother surfaces, there exists only one peak with 12 daughter droplets at $d = 101$ μm for case 2, and 9 daughter droplets at $d = 83$ μm for case 3. The distribution of the droplet number density shows more uniform with droplet size at case 4. With the increase of surface roughness, the number density distributions of the daughter droplets get more uneven, and the differences between the number of large size droplets and small size ones become more obvious.

3.4 Influence of impacting velocity

The impacting velocity is also a key parameter that affects the droplet splashing process. In this study, the velocity of the mother droplet is accelerated in the wind tunnel. To investigate the influence of the impacting velocity on droplet impact and splash, the high-speed DIH sequences, the droplet size, droplet number as well as the 3D distribution of the daughter droplets are analyzed in the following parts. In this study, the daughter droplets are captured at case 2, case 5, and case 6 with 25 μm surface roughness with different impacting velocities, 4.09 ± 0.01 m/s, 4.53 ± 0.04 m/s, and 5.02 ± 0.05 m/s, respectively. The corresponding *K* are 241, 266, and 298.

Figure 11 displays the high-speed DIH sequence of droplet impact and splashing process. The thickness of the residual top of mother droplets decreases with the impacting velocity at the 1st frame, which are 0.36 mm at case 2, 0.28 mm at case 5, and 0.16 mm at case 6, respectively. The number of the daughter droplets ejected from the expanding contact line is 92 at case 2, 163 at case 5, and 183 at case 6, which increases with the impacting velocity at the 3rd frame. When it comes to the 10th frame, the liquid layer accumulated on the solid surface lessens with the impacting velocity as you can see from the last row in Fig. 11.

Figure 12 demonstrates the 3D distribution of the daughter droplets at the 3rd frame with three different impacting velocities. To effectively analyze the influence of impacting

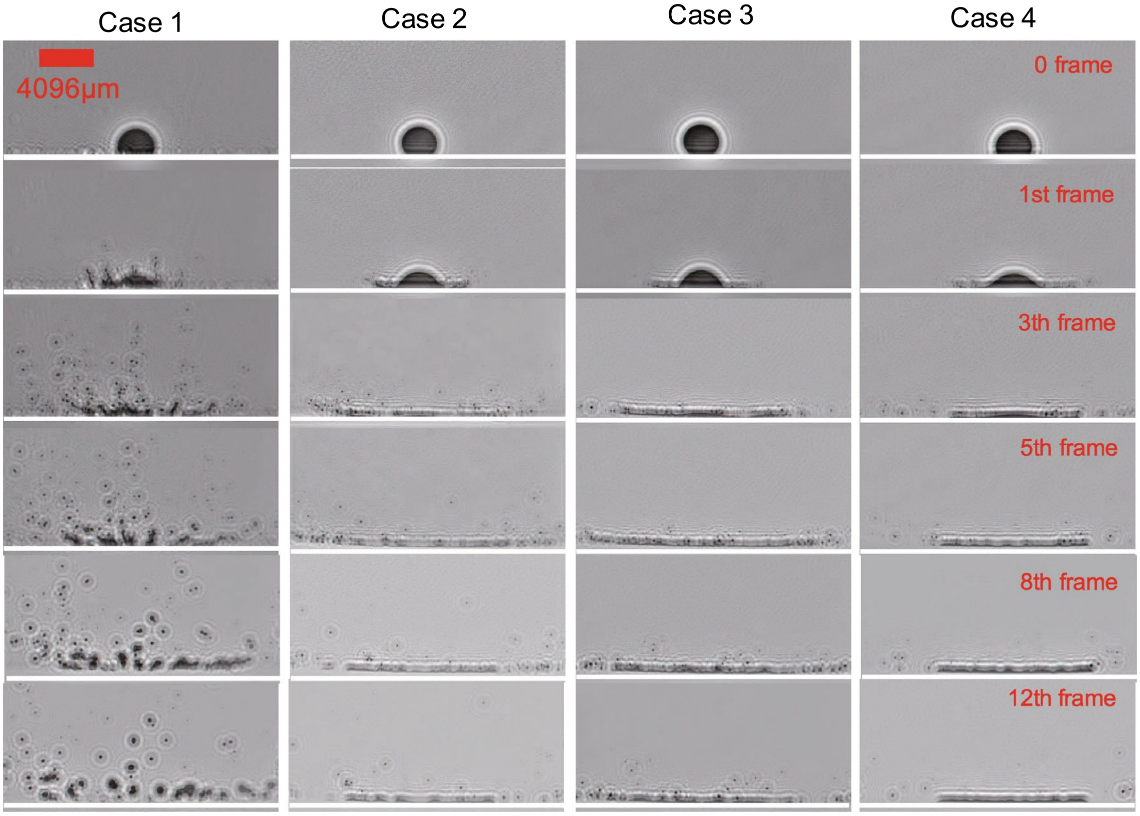

Fig. 9 The high-speed DIH sequences of droplet impact and splash under case 1, case 2, case 3, and case 4 conditions: D = 2630 ± 20 μm, V_0 = 4.09 ± 0.01 m/s, and Ra are 250 μm, 25 μm, 3.2 μm, and 2.6 μm respectively

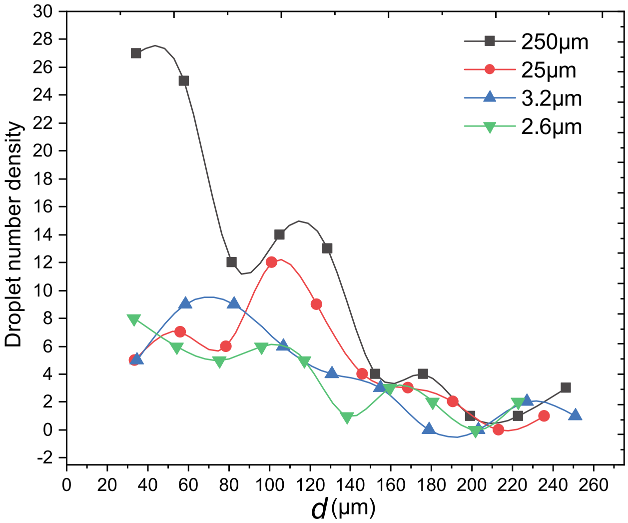

Fig. 10 The number density of the daughter droplets at four cases with the different surface roughnesses of 250 μm, 25 μm, 3.2 μm, and 2.6 μm at the 3rd frame

velocity on droplet impact and splash, the splashing phenomena with three cases are into statistical analysis when all daughter droplets are still in the view of the camera. To obtain reliable statistics, the droplet size distribution is a sum of two experiments taken under the same conditions in Fig. 12. The red balls, yellow balls and blue balls stand for the daughter droplets for case 2, case 5 and case 6, respectively. The maximum altitudes to fly for the daughter droplets at three cases are 4.78 mm, 6.46 mm and 6.94 mm. It can be seen the splashing heights of the daughter droplets increase with the impacting velocity. The $x-y$ projection of the daughter droplet 3D distribution of three cases for Fig. 12 is displayed in Fig. 13. The distribution of the daughter droplet along the x-axis for three cases are −8.23 ot 9.96 mm (distance: 18.19 mm) at case 2, −9.85 to 10.35 mm (distance: 20.20 mm) at case 5, and − 13.00 to 10.43 mm (distance: 23.43 mm) at case 6, respectively. As to the y-axis, the distribution of the daughter droplet are −10.63 to 8.15 mm (distance: 18.78 mm) at case 2, −13.3 to 11.13 mm (distance: 24.43 mm) at case 5, and −14.00 to 13.78 mm (distance: 27.78 mm) at case 6, respectively. It can be seen that the distribution of the daughter droplets along the x-axis and y-axis distinctly increases with the impacting velocity. This is because the component of momentum along the radial direction produced from the droplet impact process increases with the impacting velocity. Here is an interesting phenomenon that daughter droplets are not in an

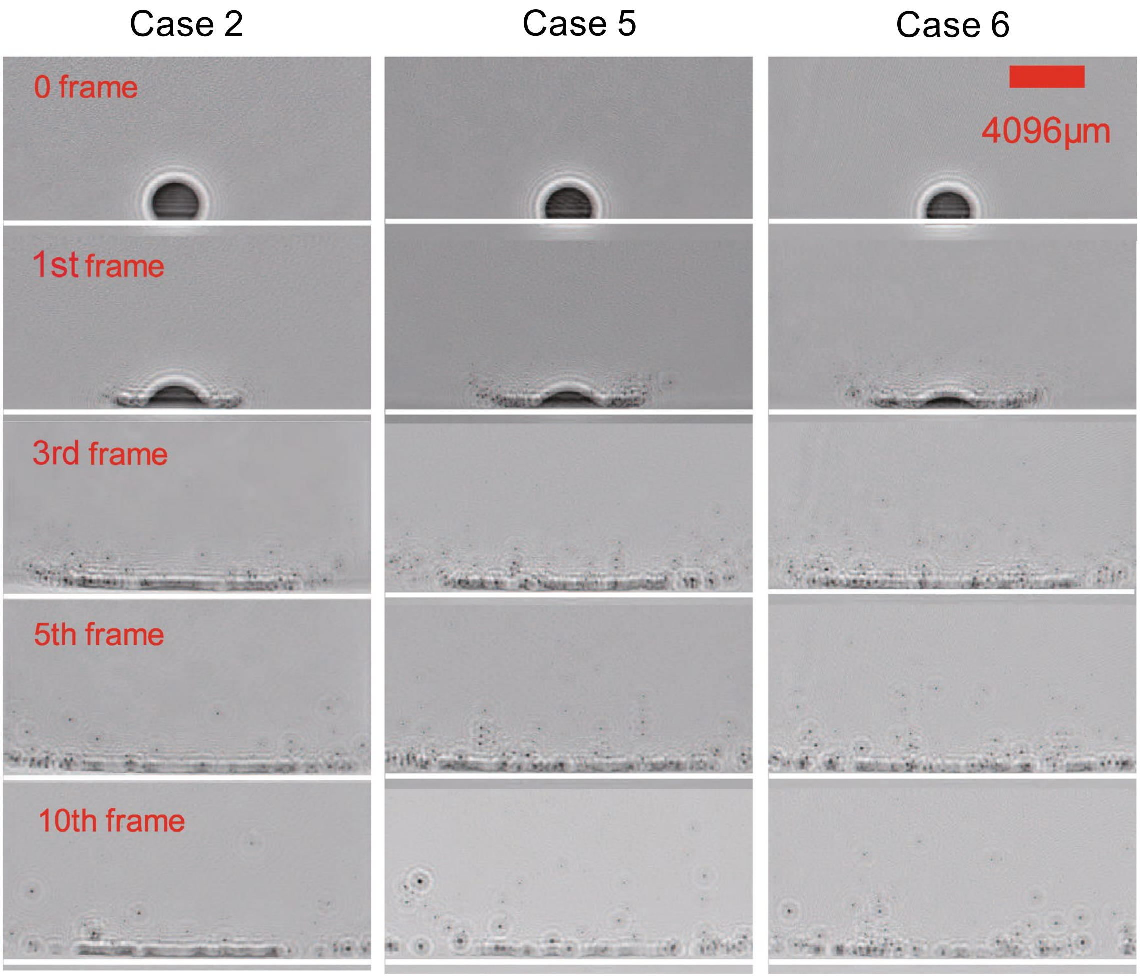

Fig. 11 The high-speed DIH sequences of droplet impact and splash under case 2, case 5, and case 6 conditions: D = 2630 ± 20 μm, Ra = 25 μm, and V_0 = 4.09 ± 0.01 m/s, 4.53 ± 0.04 m/s and 5.02 ± 0.05 m/s, respectively

axisymmetric distribution along the x-axis and y-axis at all three cases.

To investigate the asymmetrical distribution of the daughter droplets, the droplet number and mass loss rate (V_{dt}/V_D *100%) for three cases at the 3rd frame are analyzed and demonstrated in Fig. 14, where V_{dt} is the total volume of the all daughter droplets and V_D is the volume of the mother droplet. The result shows that the number of the daughter droplets and the mass loss are increasing with the impacting velocity from 4.09 ± 0.01 m/s to 4.53 ± 0.04 m/s. As the impacting velocity increases from 4.53 ± 0.04 to 5.02 ± 0.05 m/s, the number of the daughter droplets increase from 80 to 110 at the negative x-axis, and from 52 to 73 at the the positive y-axis. However, the trend of the mass loss rate changing with the impacting velocity is different with that of the number of the daughter droplets at the negative x-axis. It means that the mass loss rate has a non-linear relationship with the number of the daughter droplets, and the diameters of the daughter droplets at the negative x-axis are larger than those at the positive x-axis. According to the daughter droplet distribution of droplet impact with different velocities in Fig. 13, the number of large droplets greater than 200 μm matches with the trend of the mass loss

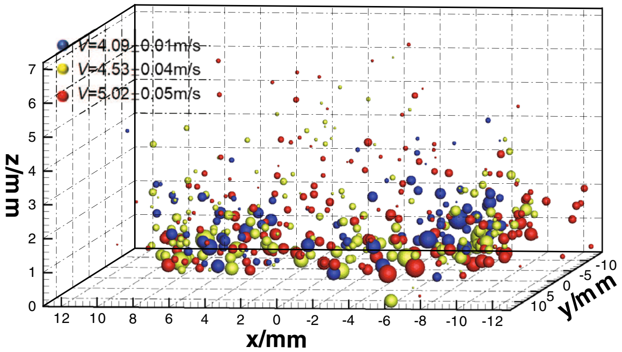

Fig. 12 The 3D distribution of the daughter droplets at the 3rd frame of three cases for Fig. 11

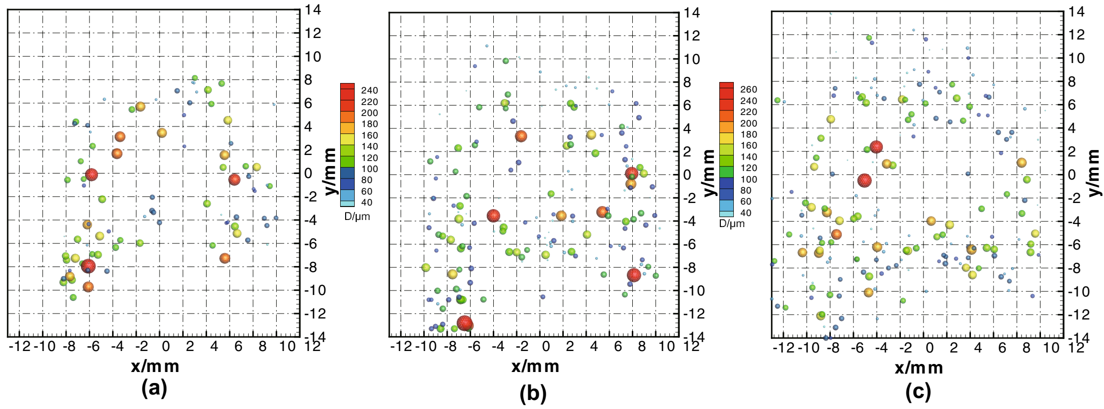

Fig. 13 The $x-y$ projection of the daughter droplet 3D distribution of three cases for Fig. 12

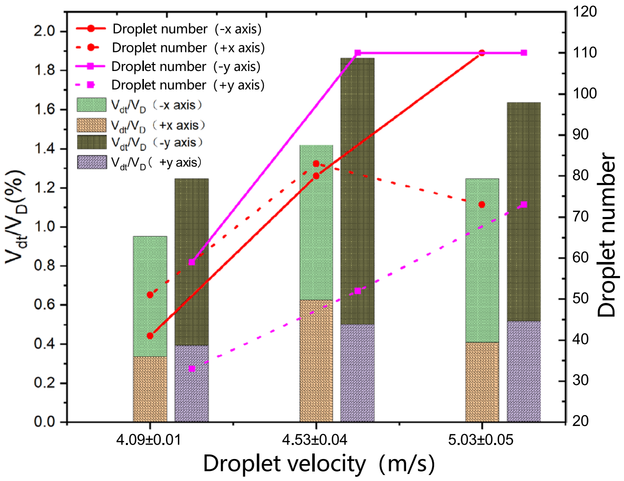

Fig. 14 The number of the daughter droplets and mass loss rate at the positive x-axis and y-axis, as well as at the negative x-axis and y-axis for three cases in Fig. 11

rate, which generated from the rupture of the liquid filaments detached from the wall in droplet breakup mode 3, increasing with the impacting velocity from 4.09 ± 0.01 to 4.53 ± 0.04 m/s. When it comes to the case at the impacting velocity of 5.02 ± 0.05 m/s, the number of the larger droplets decreases resulting in a slightly lower mass loss rate.

The mass loss rate of droplet splash at the positive y-axis is obviously less than that at the negative y-axis for all three cases. The differences in the number of the daughter droplets on both sides of the y-axis are 26 at case 2, 58 at case 5 and 37 at case 6, respectively. The number of the daughter droplets at the positive x-axis are close to those at the negative x-axis at case 2 and case 5. While it shows distinct difference at case 6, whose number difference is 37. This phenomenon can be contributed to that the daughter droplet distribution is affected by the asymmetry of the flow field of the wind tunnel along the x-axis and y-axis. So the daughter droplets show different distributions for these two axises. The results indicate that the daughter droplets show a distinct asymmetric distribution of the daughter droplet number and mass loss rate in 3D position.

4 Conclusion

Experiments of the large droplet (2630 ± 20 μm) impacting different rough surfaces with the impacting velocities of 4.09 ± 0.01 m/s, 4.53 ± 0.04 m/s, and 5.02 ± 0.05 m/s are carried out in a wind tunnel at 15°C. The splashing characteristics of the emitted daughter droplets are captured and analyzed with high-speed DIH at 3500 Hz. The conclusions and outlook can be made as to the following points:

(1) The high-speed DIH has been proved to have distinct advantage of clearly capturing the droplet morphology evolution during the droplet impact and splashing process. The droplet sizes and 3D positions of the daughter droplets can be also visualized. The 3D motion trajectory of the daughter droplets can be achieved by applying a four consecutive frames particle tracking algorithm based on particle matching probability, which can help to predict the secondary impact points of the daughter droplets. The result shows that there exist three kinds of droplet breakup modes during the droplet impact and splashing process. Droplet breakup mode 1 shows that the small daughter droplets eject from the crush of the cusps of free rim; some small daughter droplets and large daughter droplets produce in droplet breakup mode 2, where the jets of free rim rupture into the daughter droplets; other large droplets mainly result from the breakage of the liquid filaments detached from the surface, which is called droplet breakup mode 3.

(2) The influence of surface roughness on droplet splashing characteristics is studied by comparing the droplet

morphology evolution and the number of the daughter droplets during the droplet impact and splashing process. The results show that the mother droplet, which impinges a solid surface with larger roughness, undergoes a more violent splashing process. The number of the daughter droplets at the 3rd frame increases with the surface roughness, which are 104, 49, 39, and 38 when the surface roughnesses are 250 μm, 25 μm, 3.2 μm and 2.6 μm, respectively. The number density distributions of the daughter droplets become more uniform with the increase of surface roughness.

(3) The influence of impacting velocity on droplet splashing characteristics is also analyzed by comparing the morphology, 3D position, droplet number distribution of the daughter droplets. The statistical results indicate that there is significantly more intense splashing process at higher impacting velocity. The farthest distance of droplet distribution gradually increases with impacting velocity because of the larger component of momentum in the radial direction, which are 18.19 mm (4.09 ± 0.01 m/s), 20.20 mm (4.53 ± 0.04 m/s) and 23.43 mm (5.02 ± 0.05 m/s) along the x-axis, as well as 18.78 mm (4.09 ± 0.01 m/s), 24.43 mm (4.53 ± 0.04 m/s) and 27.78 mm (5.02 ± 0.05 m/s) along the y-axis. The daughter droplets are not in radially symmetric distribution of the droplet number and mass loss rate for the reason of an asymmetry distribution of the flow field of the wind tunnel along the x-axis and y-axis.

3D visualization and investigation with High-speed DIH system can provide an insight into the 3D splashing characteristics and asymmetric distribution along the x-axis and y-axis of the daughter droplets, which can be applied to validate and improve the existing 3D models in the future.

Supplementary Information The online version contains supplementary material available at https://doi.org/10.1007/s00348-022-03416-7.

Acknowledgements The authors thank the financial support from National Natural Science Foundation of China (52006193), Natural Science Foundation of Zhejiang Province (LQ19E060010), National Science and Technology Major Project (2017-V-0016-0069), National Key Research and Development Program of China (2020YFA0405700, 2020YFB0606201), and Open Fund of Key Laboratory of Icing and Anti/De-icing (Grant No. IADL2019XXXX).

References

Adam CD (2013) Experimental and theoretical studies of the spreading of bloodstains on painted surfaces. Forensic Sci Int 229(1–3):66–74

Bhushan B (2000) Surface roughness analysis and measurement techniques. Modern tribology handbook. CRC Press, Florida, pp 79–150

Biroun MH, Rahmati M, Tao R, Torun H, Jangi M, Fu Y (2020) Dynamic behavior of droplet impact on inclined surfaces with acoustic waves. Langmuir 36(34):10175–10186

Blossey R (2003) Self-cleaning surfaces-virtual realities. Nat Mater 2(5):301–306

de Goede T, de Bruin K, Shahidzadeh N et al (2021) Droplet splashing on rough surfaces. Phys Rev Fluids 6(4):043604

Gao J, Guildenbecher DR, Reu PL, Kulkarni V, Sojka PE, Chen J (2013) Quantitative, three-dimensional diagnostics of multiphase drop fragmentation via digital in-line holography. Opt Lett 38(11):1893–1895

Hao J, Green SI (2017) Splash threshold of a droplet impacting a moving substrate. Phys Fluids 29(1):012103

Henneberger J, Fugal JP, Stetzer O, Lohmann U (2013) HOLIMO II: a digital holographic instrument for ground-based in situ observations of microphysical properties of mixed-phase clouds. Atmos Meas Tech 6(11):2975–2987

Heyman J (2019) TracTrac: a fast multi-object tracking algorithm for motion estimation. Comput Geosci 128:11–18

Josserand C, Thoroddsen ST (2016) Drop impact on a solid surface. Annu Rev Fluid Mech 48:365–391

Khavari M, Sun C, Lohse D, Tran T (2015) Fingering patterns during droplet impact on heated surfaces. Soft Matter 11(17):3298–3303

Khojasteh D, Kazerooni M, Salarian S, Kamali R (2016) Droplet impact on superhydrophobic surfaces: a review of recent developments. J Ind Eng Chem 42:1–14

Kim J (2007) Spray cooling heat transfer: the state of the art. Int J Heat Fluid Flow 28(4):753–767

Koch K, Grichnik R (2016) Influence of surface structure and chemistry on water droplet splashing. Philos Trans R Soc A Math Phys Eng Sci 374(2073):20160183

Latka A, Strandburg-Peshkin A, Driscoll MM, Stevens CS, Nagel SR (2012) Creation of prompt and thin-sheet splashing by varying surface roughness or increasing air pressure. Phys Rev Lett 109(5):054501

Lin X, Wu Y, Wu C, Yao L, Wu X, Chen L, Cen K (2019) Evolution of volatile cloud in pulverized coal combustion with high-speed digital inline holographic visualization. Fuel 241:199–206

Liu K, Jiang L (2012) Bio-inspired self-cleaning surfaces. Annu Rev Mater Res 42:231–263

Liu Y, Andrew M, Li J, Yeomans JM, Wang Z (2015) Symmetry breaking in drop bouncing on curved surfaces. Nat Commun 6(1):1–8

Longchao Y (2019) Digital holographic method and application to measurement of particle combustion and droplet atomization. Zhejiang University

Mundo CHR, Sommerfeld M, Tropea C (1995) Droplet-wall collisions: experimental studies of the deformation and breakup process. Int J Multiph Flow 21(2):151–173

Potapczuk M (2003) Ice mass measurements: implications for the ice accretion process. In: 41st Aerospace sciences meeting and exhibit. p 387

Range K, Feuillebois F (1998) Influence of surface roughness on liquid drop impact. J Colloid Interface Sci 203(1):16–30

Rioboo R, Tropea C, Marengo M (2001) Outcomes from a drop impact on solid surfaces. Atom Sprays 11(2)

Roisman IV, Opfer L, Tropea C, Raessi M, Mostaghimi J, Chandra S (2008) Drop impact onto a dry surface: role of the dynamic contact angle. Colloids Surf A 322(1–3):183–191

Scheller BL, Bousfield DW (1995) Newtonian drop impact with a solid surface. AIChE J 41(6):1357–1367

Tang C, Qin M, Weng X, Zhang X, Zhang P, Li J, Huang Z (2017) Dynamics of droplet impact on solid surface with different roughness. Int J Multiph Flow 96:56–69

Thoroddsen ST, Takehara K, Etoh TG (2012) Micro-splashing by drop impacts. J Fluid Mech 706:560–570

Vander Wal RL, Berger GM, Mozes SD (2006) The splash/non-splash boundary upon a dry surface and thin fluid film. Exp Fluids 40(1):53–59

Villermaux E, Bossa B (2011) Drop fragmentation on impact. J Fluid Mech 668:412

Wang YP, Wilkinson GB, Drallmeier JA (2004) Parametric study on the fuel film breakup of a cold start PFI engine. Exp Fluids 37(3):385–398

Wang MJ, Lin FH, Ong JY, Lin SY (2009) Dynamic behaviors of droplet impact and spreading-Water on glass and paraffin. Colloids Surf A 339(1–3):224–231

Wischmeier WH, Smith DD (1958) Rainfall energy and its relationship to soil loss. EOS Trans Am Geophys Union 39(2):285–291

Worthington AM (1877) XXVIII. On the forms assumed by drops of liquids falling vertically on a horizontal plate. Proc R Soc London 25(171–178):261–272

Wu Y, Wu X, Yao L, Gréhan G, Cen K (2015) Direct measurement of particle size and 3D velocity of a gas-solid pipe flow with digital holographic particle tracking velocimetry. Appl Opt 54(9):2514–2523

Wu Y, Wu X, Yao L, Brunel M, Coëtmellec S, Lebrun D, Cen K (2016) 3D boundary line measurement of irregular particle with digital holography. Powder Technol 295:96–103

Wu X, Lin X, Yao L, Wu Y, Wu C, Chen L, Cen K (2019) Primary fragmentation behavior investigation in pulverized coal combustion with high-speed digital inline holography. Energy Fuels 33(9):8126–8134

Xu L, Zhang WW, Nagel SR (2005) Drop splashing on a dry smooth surface. Phys Rev Lett 94(18):184505

Xu L, Barcos L, Nagel SR (2007) Splashing of liquids: interplay of surface roughness with surrounding gas. Phys Rev E 76(6):066311

Yao L, Wu X, Wu Y, Yang J, Gao X, Chen L, Cen K (2015) Characterization of atomization and breakup of acoustically levitated drops with digital holography. Appl Opt 54(1):A23–A31

Yarin AL (2006) Drop impact dynamics: splashing, spreading, receding, bouncing. Annu Rev Fluid Mech 38:159–192

Yingchun W, Xuecheng W, Jing Y, Zhihua W, Xiang G, Binwu Z, Kefa C (2014) Wavelet-based depth-of-field extension, accurate autofocusing, and particle pairing for digital inline particle holography. Appl Opt 53(4):556–564

Zable JL (1977) Splatter during ink jet printing. IBM J Res Dev 21(4):315–320

Authors and Affiliations

Xiaodan Lin[1] · Qiao Wang[2] · Yingchun Wu[1] · Longchao Yao[1] · Zhiliang Xue[1] · Xuecheng Wu[1]

✉ Yingchun Wu
wuyingchun@zju.edu.cn

[1] State Key Laboratory of Clean Energy Utilization, Zhejiang University, Hangzhou 310027, China

[2] School of Mechanical and Aerospace Engineering, Kingston University London, London SW15 3DW, UK